Synthesis, structure, optical, and electric properties of Ce-doped $CuInTe_2$ compound*

Fu Li(付 丽) and Guo Yong-Quan(郭永权)†

School of Energy Power and Mechanical Engineering, North China Electric Power University, Beijing 102206, *China*

(Received 4 May 2014; revised manuscript received 14 July 2014; published online 10 October 2014)

Ce-doped $CuInTe_2$ (CICT) semiconducting compounds are successfully synthesized. The phase structures, optical, and electric properties are investigated using powder X-ray diffraction (XRD), field emission scanning electron microscopy (FESEM), X-ray photoelectron spectrometer (XPS), Raman spectrometer, ultraviolet and visible spectrophotometer (UV-Vis), and a standard four-probe method. $CuIn_{1-x}Ce_xTe_2$ crystallizes into a tetragonal structure with predominant orientation along the [112] direction. The lattice parameters are $a = 6.190(6)$ Å–6.193(0) Å and $c = 12.406(5)$ Å–12.409(5) Å. Ce prefers to occupy the 4*b* crystal position. According to the analysis of XPS spectra, Ce shows the mixture of valences 4+ and 3+. Raman spectra reveal that the photon vibrating model in the CICT follows A_1 mode in a wavenumber range of 123 cm^{-1}–128 cm^{-1}. UV-Vis spectra show that the band gap E_g values before and after 0.1 mole Ce doped into $CuInTe_2$ are 1.28 eV and 1.16 eV, respectively. It might be due to the mixture of valences for Ce. Ce doped into $CuInTe_2$ still shows the semiconductor characteristics.

Keywords: $CuIn_{1-x}Ce_xTe_2$, chalcopyrite, Raman spectrum, band gap, semiconductor

PACS: 78.20.–e, 61.50.–f, 71.15.Ap, 72.20.–i **DOI:** 10.1088/1674-1056/23/12/127801

1. Introduction

I–III–VI_2 ternary compound with chalcopyrite structures have been extensively studied due to their applications in photovoltaic cells.[1–5] $CuInSe_2$ solid solution with Ga substitution for In, and S substitution for Se, commonly referred to as $Cu(In,Ga)(Se,S)_2$ (CIGS),[6,7] is a leading candidate material of solar cells because of its high photoelectric transformation efficiency of 20.3%.[8] Since Te also belongs to VI group, the tellurium-based semiconductor with a chalcopyrite structure is widely investigated for its potential application in solar cells.[9,10] $CuInTe_2$ (CIT) film shows an excellent photoelectric property and has the potential application as one of the competent absorber materials in the photovoltaic devices. $CuInTe_2$ has a smaller direct band gap, a stronger quantum confinement effect and a larger Bohr radius than those of CIGS, $CuInSe_2$, and $CuInS_2$. $CuInTe_2$ with a band gap ranging from 0.96 eV to 1.04 eV is well-adapted to the absorption of solar spectra, and its optical absorption coefficient (10^5 cm^{-1}) is suitable for application in solar cells.[11,12]

The rare-earth ions-doped semiconductors have been used in some luminescent and fluorescent devices due to their specific 4f electronic structures of rare-earth element and unique optical properties such as high quantum efficiencies of absorption light at short wavelength and subsequent emission light at long wavelength.[13–17] However, the studies on the rare-earth-doped $CuInSe_2$ semiconductors are very limited,[18,19] to date there has been no report on the rare-earth-element-doped $CuIn_{1-x}R_xTe_2$ (CIRT) semiconductors. Based on the formation mechanism of a p–n junction in a semiconductor, the p-type semiconductor could form by doping electron-rich impurities. Since cerium ion with 4+ could supply one electron compared with Ce^{3+}, the rare-earth element with high valence state, doped into a semiconductor, induces an electron-type semiconductor. The formation mechanism could also be used to understand the n-type semiconductor by doping rare earth with a low valence state. If the n–p junction controlled by rare earth could be used in CIGS solar cells, the toxic CdS layer with an n-type semiconductor should be replaced in cells in order to reduce the pollution in air. In addition, the rare earth element with various valences, doped into CIRT for matching co-lattice and reducing defects in thin-film, is beneficial for the binding stability of p–n junction.

In this paper, the cerium-doped $CuIn_{1-x}Ce_xTe_2$ compounds are prepared and their structures, photon vibrating modes, optical and electric properties are systemically studied. To our knowledge, this is the first report on the study of Ce doping effects on structure and photo-electric properties in CIT.

2. Experimental procedure

The raw materials of Cu and In granules (> 99.99% Sigma Aldrich), and fine chips of Te and Ce (> 99.99% Aldrich) were used for preparing the CICT semiconductor. $CuIn_{1-x}Ce_xTe_2$ (where $x = 0$, 0.1, 0.2, 0.3) compounds were prepared by arc-melting in an atmosphere of ultra-pure argon gas with an excess of 10% tellurium for the compensation of

*Project supported by the National Natural Science Foundation of China (Grant No. 11274110).

†Corresponding author. E-mail: yqguo@ncepu.edu.cn

© 2014 Chinese Physical Society and IOP Publishing Ltd

evaporation loss of tellurium during melting. To ensure the homogeneity, the ingots of CICT were turned upside down and re-melted four times.

The field emission scanning electron microscopy (FE-SEM JSM-7001F) equipped with energy dispersive X-ray spectroscopy (EDS) were used to investigate the surface morphologies and check the element compositions of CICT. A Rigaku G/max 2500 powder X-ray diffractometer with Cu radiation was employed to check the phase structure in CICT. Rietveld's diffraction profile-fitting technique was utilized to determine the lattice parameters and atomic occupations. ESCALAB 250Xi X-ray photoelectron spectrometer (XPS) was used for checking the valence state of Ce in CICT. HR800 model laser Raman spectrometer in the backscattering geometry used with an Si charge couple device detector was employed to study the photon vibrations.

The absorption rate dependence of the wavelength for $CuIn_{1-x}Ce_xSe_2$ was investigated using a Shimadzu 2450 UV-Vis spectrophotometer with scanning ranging from 300 nm to 800 nm and in scanning steps of 1 nm/sec. Finally the resistivity of $CuIn_{1-x}Ce_xSe_2$ was measured using a standard four-probe technique in a temperature range from 5 K to room temperature.

3. Results and discussion

3.1. FESEM observations

Cerium content dependences of SEM morphologies for $CuIn_{1-x}Ce_xTe_2$ ($x = 0$, 0.1, 0.2, 0.3) are shown in Figs. 1(a)–1(d), respectively. The growths of grain exhibit inhomogeneity from large bulks to small pieces with grain sizes ranging from 200 nm to 5 μm. The morphologies on the grain surfaces reveal the evolutions of growth of the grains on the surfaces from the initial triangle facet with smooth and uniformity (Fig. 1(a)) and large granularity with sharp edges (Fig. 1(b)) to the cylindrical and layer structures (Figs. 1(c) and 1(d)). The grain sizes tend to decrease with the increase of cerium content in the CICT semiconductor. The bulk grains are initially packed into layer structures. With the decease of grain size, the small cylindrical crystals grow. It shows that the rare-earth cerium is helpful for refining the grains.

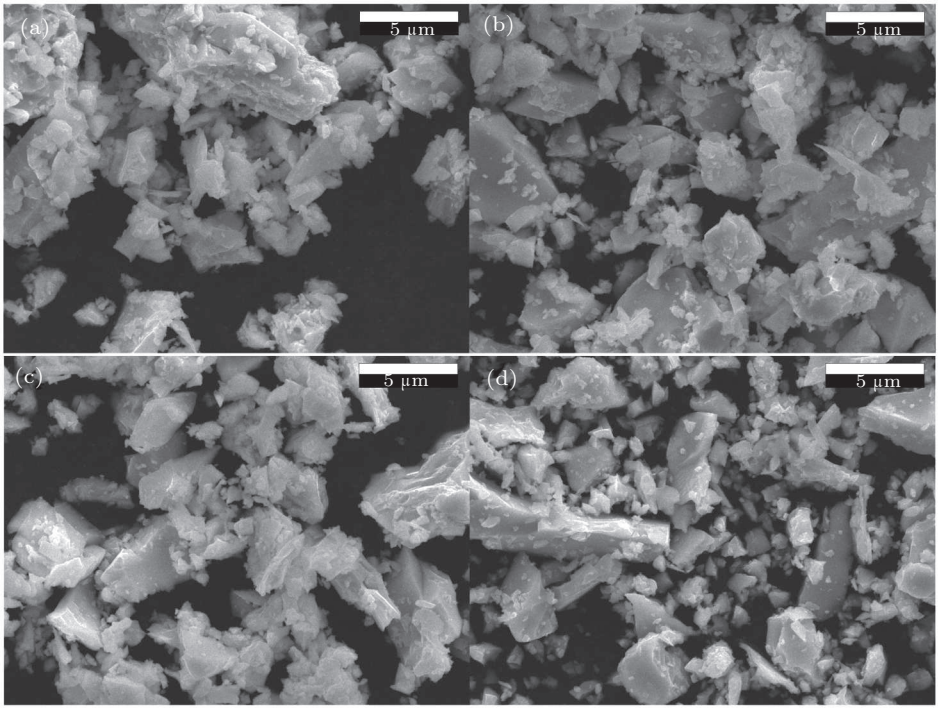


Fig. 1. FESEM micrographs of CICT with Ce content $x = 0$ (a), 0.1 (b), 0.2 (c), and 0.3 (d).

Table 1. Quantitative atomic compositions in CICT detected by EDS

$CuIn_{1-x}Ce_xTe_2$	[Cu]/at.%		[In]/at.%		[Ce]/at.%		[Te]/at.%	
	Theo	Exp	Theo	Exp	Theo	Exp	Theo	Exp
$x = 0$	25.00	25.57	25.00	26.12	0	0	50.00	48.31
$x = 0.1$	25.00	25.44	22.50	24.47	2.50	1.82	50.00	48.27
$x = 0.2$	25.00	24.70	20.00	24.31	5.00	2.24	50.00	48.75
$x = 0.3$	25.00	23.56	17.50	24.25	7.50	4.70	50.00	47.49

The element compositions in CICT are evaluated by EDS. The characteristic spectra of Cu_K, In_L, Ce_L, and Te_L are presented in Table 1. The measurements show that the compositions of cerium and tellurium are lower than those in stoichiometric $CuIn_{1-x}Ce_xTe_2$ due to their evaporations in the arc melting process.

3.2. X-ray diffraction analysis

The X-ray diffraction (XRD) patterns of $CuIn_{1-x}Ce_xTe_2$ ($x = 0$, 0.1, 0.2, 0.3) are shown in Fig. 2. The diffraction peaks could be indexed as a tetragonal structure according to the results of the TREOR program. The planar indices follow the extinction rules of the chalcopyrite $CuInTe_2$ (ICDD-01-082-0450) with a space group of I-42d. A single phase of $CuInTe_2$ is detected in CICT, except that a small amount of (In, Cu)Te as impurity exists in $CuIn_{0.9}Ce_{0.1}Te_2$ as marked in Fig. 2. The diffraction characteristic peaks of (1 1 2), (2 0 4)/(2 2 0), (3 1 2)/(1 1 6), (3 1 6)/(3 3 2), (4 0 0), and (4 2 4) planes in the chalcopyrite structure are observed for the CICT samples.

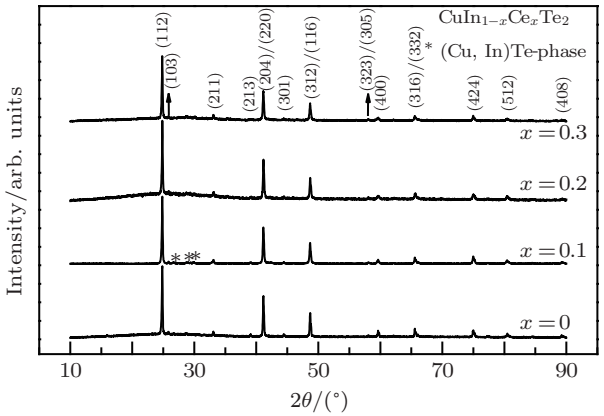


Fig. 2. XRD patterns of CICT compounds.

The refined XRD patterns of CICT compounds are shown in Fig. 3, where the '+' symbols represent the experimental data; the solid lines represent the calculated pattern, and the lowest lines indicate the difference between the calculated and experimental patterns. The calculated patterns agree with the measured ones well.

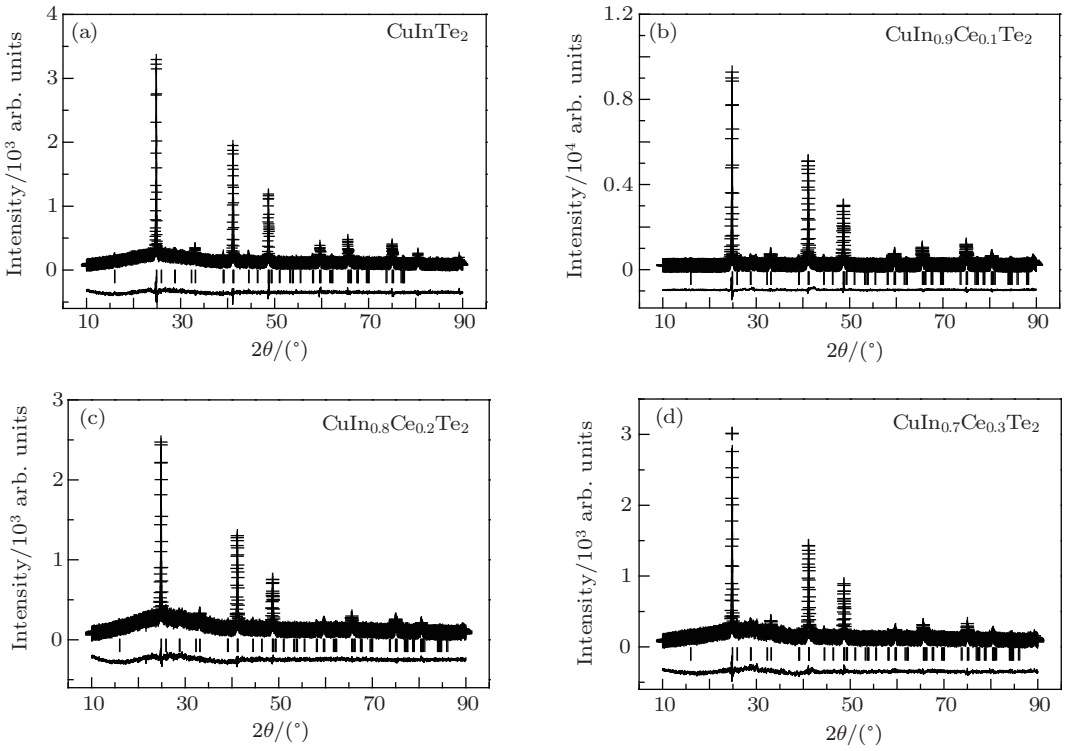


Fig. 3. Refinement XRD patterns of CICT compounds.

Table 2 lists the structural parameters, atomic positions, and residual factors of the $CuInTe_2$ phase in CICT, and Table 3 lists the structural parameters, atomic positions, and residual factors of (Cu, In)Te impurity phase in $CuIn_{0.9}Ce_{0.1}Te_2$. The space group of $CuInTe_2$ phase is I-42d, and the lattice parameters are $a = 6.190(6)$ Å–6.193(0) Å and $c = 12.406(5)$ Å–12.409(5) Å. The parameters a and c in Ce-doped CICT are larger than those in CIT, which means that Ce can be substituted for In in $CuInTe_2$, for the radius of Ce is slightly larger than that of In. The atomic occupations correspond to the 4a (0, 0, 0) crystal site for Cu, the 4b (0, 0, 0.5) site for In, and the 8d (x, 0.25, 0.125) site for Te. Additionally, Rietveld refinements confirmed that the $CuInTe_2$ phase has a tetragonal chalcopyrite structure with an orientation predominantly along

the [112] direction. According to Ref. [20], the content of the impurity phase can be determined from the refinement results by the following formula:

$$W_i = \frac{Z_i M_i V_i S_i}{\sum (Z_i M_i V_i S_i)}, \quad (1)$$

where W_i is the weight percentage of the i-th phase, Z_i, M_i, V_i, and S_i represent the number of formula units in a unit cell, molecular weight, cell volume, and scale factor of the i-th phase, respectively. Based on this model, the phase content of (Cu, In)Te impurity in $CuIn_{0.9}Ce_{0.1}Te_2$ is 3.46 wt%.

Table 2. Refined lattice parameters of $CuIn_{1-x}Ce_xTe_2$.

	$CuInTe_2$ type in $CuIn_{1-x}Ce_xTe_2$			
Parameters	$x = 0$	$x = 0.1$	$x = 0.2$	$x = 0.3$
a	6.1906	6.1930	6.1910	6.1918
c	12.4065	12.4095	12.4084	12.4094
V	475.46	475.94	475.60	475.76
Cu (4a)	(0,0,0)	(0,0,0)	(0,0,0)	(0,0,0)
In/Ce (4b)	(0,0,1/2)	(0,0,1/2)	(0,0,1/2)	(0,0,1/2)
Te (8d)	(0.22290,1/4,1/8)	(0.22269,1/4,1/8)	(0.21811,1/4,1/8)	(0.21782,1/4,1/8)
R_{wp}	11.767	8.715	12.398	12.207
R_p	9.296	6.510	9.725	9.576

Table 3. Refined lattice parameters of (Cu, In)Te in $CuIn_{0.9}Ce_{0.1}Te_2$.

(In, Cu)Te type in $CuIn_{0.9}Ce_{0.1}Te_2$	
a	8.4427
c	7.1266
V	507.87
In (4a)	(0,0,1/4)
Cu/In (4b)	(0,1/2,1/4)
Te (8h)	(0.19587,0.69587,0)

Based on the refined results, the typical crystal structure of $CuInTe_2$ is drawn with Diamond software, and shown in Fig. 4. The nearest bond lengths and bond angles in $CuInTe_2$ are listed in Table 4. The bond length of Cu–Te decreases and that of In–Te increases with the increase of Ce content as a result of the substitution of Ce atoms for part of In atoms.

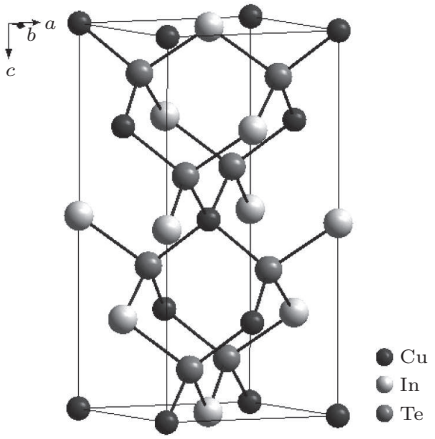


Fig. 4. Crystal structural frame of $CuInTe_2$ with chalcopyrite structure.

Table 4. Bond lengths and bond angles in $CuInTe_2$.

	$CuInTe_2$						
$CuIn_{1-x}Ce_xTe_2$	Bond length/Å		Bond angle/(°)				
	Cu–Te	In–Te	Cu–Te–Cu	Cu–Te–In	In–Te–In	Te–Cu–Te	Te–In–Te
$x = 0$	2.5893	2.7826	115.594	109.097 109.262	103.881	111.022 106.412	112.258 108.096
$x = 0.1$	2.5894	2.7844	115.638	109.101 109.254	103.835	111.030 106.397	112.288 108.081
$x = 0.2$	2.5738	2.8012	116.713	108.992 109.164	102.928	111.294 105.884	112.757 107.854
$x = 0.3$	2.5732	2.8027	116.780	108.988 109.156	102.870	111.309 105.855	112.790 107.838

3.3. XPS analysis

A typical XPS spectrum for Ce-rich $CuIn_{1-x}Ce_xTe_2$ is presented in Fig. 5. The characteristic peaks are observed at 873.6, 882.5, 885.3, 898.5 eV for Ce $3d_{5/2}$ and 903.8 eV and 916.9 eV for Ce $3d_{3/2}$, respectively. It confirms the existence of Ce^{4+} and Ce $^{3+}$ in CICT. Thus, the valence of Ce in CICT powders can be described as a mixture valence of 4+ and 3+, and the main valence of Ce in the compound is 4+.

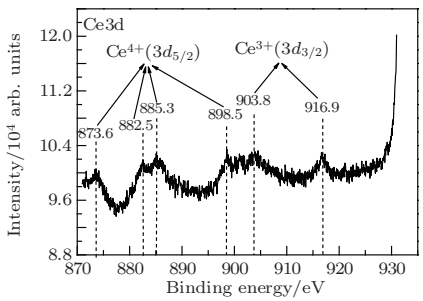


Fig. 5. Ce 3d region of XPS spectrum for $CuIn_{0.7}Ce_{0.3}Te_2$ powders.

3.4. Raman spectra

The Raman characteristic spectra are sensitive to the crystal quality and structural quality of the CICT samples. The primitive unit cell of the tetragonal chalcopyrite structure (space group I-42d) contains two molecules with eight atoms. These can give rise to 24 modes of vibration, which include 21 optical and 3 acoustic modes. In the zone center, the optical modes transform as[21] $1A_1 + 2A_2 + 3B_1 + 3B_2 + 6E$, in which A_2 mode is inactive optically and only B_2 and E modes are infrared-active. Thus, all the modes, with the exception of A_2, are Raman-active.[22]

Since the CICT compound crystallizes into a chalcopyrite structure, its space group is I-42d. Therefore, it is expected that the vibrational spectra of these chalcopyrite compounds should be very similar to those in pure CIT.[23] Raman spectra of CICT compounds at ambient temperature are between 80 cm^{-1} and 400 cm^{-1} and presented in Fig. 6. The symmetry assignments of all the modes observed in CICT are summarized in Table 5. Several models reported in Refs. [24]–[26] for the chalcopyrite $CuInTe_2$ are also supplied for reference. It is observed that Raman lines for all CICT compounds appear very nearly at the same wavenumber, and are in good agreement with those reported in Refs. [23]–[25]. Hence, we assign to these lines the same symmetry.

In Fig. 6, Raman lines at 106 cm^{-1} and 126 cm^{-1} are observed for all samples. The lines around 105 cm^{-1}–107 cm^{-1} are assigned to B_2 mode according to Refs. [24] and [25]. The strongest lines appear at 127 cm^{-1}, 128 cm^{-1}, 126 cm^{-1}, 123 cm^{-1} for CICT with $x = 0, 0.1, 0.2, 0.3$, respectively. This is evidently due to the totally symmetric A_1 mode in which these strongest lines are generally observed in the Raman spectra of the chalcopyrites.[27] This mode originates from the motion of the Te atom with Cu and In atoms remaining at rest.[21] Its frequency is essentially determined by the strengths of the Cu–Te and In–Te bonds, respectively, and is nearly independent of the polarization of the incident radiation. Based on the approximation, the vibrating frequencies in chalcopyrite mainly depend on the bond-stretching forces between the nearest-neighbor atoms. A simplified version of the Keating's model is proposed by Neumann.[28] According to this model, the vibrating frequency is calculated from the following expression:

$$\nu = [2(\alpha_A + \alpha_B)/M_{Te}]^{1/2}, \tag{2}$$

where M_{Te} is the tellurium mass, the frequency of the A_1 mode in $CuInTe_2$ is 127 cm^{-1}. This coincides with the observed lines in CICT.

On the other hand, the lines at 169 cm^{-1}, 175 cm^{-1}, and 299 cm^{-1} observed in ternary compound $CuInTe_2$ are all assigned to E and/or B_2 modes, according to Refs. [24] and [25]. These lines can be detected only in $CuInTe_2$, but not in CICT. This can be explained as being due to the reduction of the cation–anion stretching force, for the substitution of Ce for In causes the extension of Te–(In, Ce) and weakens the bonding strength. Accurate positions for these characteristic lines in the specimen also match those observed in the single crystal $CuInTe_2$, which rules out the presence of the second phase. This result is in good agreement with Rietveld refinement analysis.

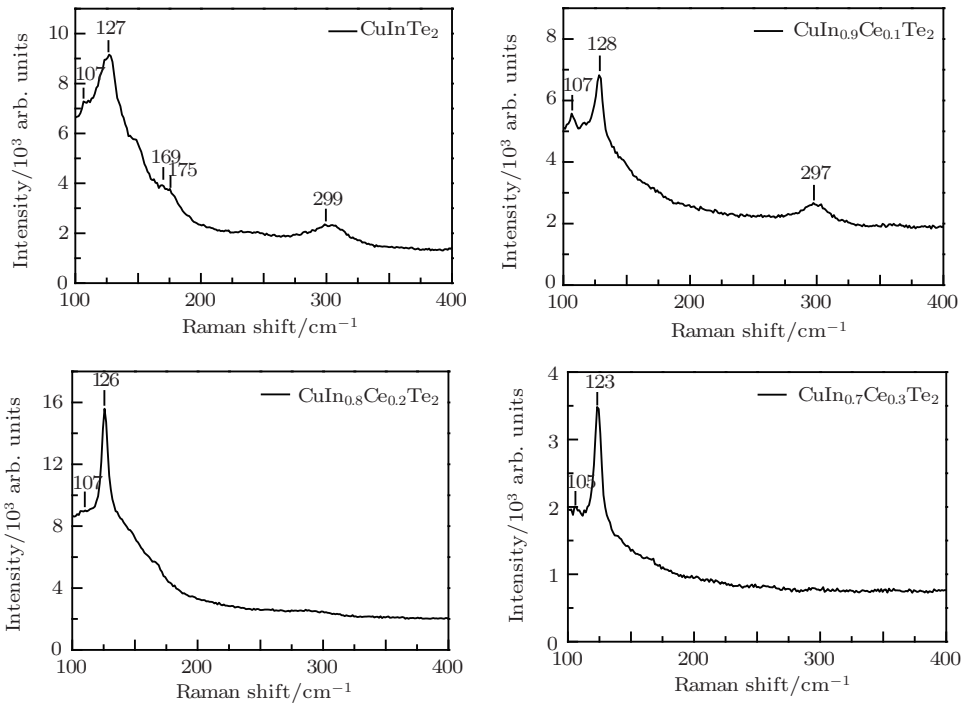


Fig. 6. Raman spectra of $CuIn_{1-x}Ce_xTe_2$ at ambient temperature in a frequency range from 80 cm^{-1} to 400 cm^{-1}.

Table 5. Phonon modes observed in $CuIn_{1-x}Ce_xTe_2$ by Raman spectra at ambient temperature

$x = 0/cm^{-1}$	$x = 0.1/cm^{-1}$	$x = 0.2/cm^{-1}$	$x = 0.3/cm^{-1}$	Modes assigned	Literature data of $CuInTe_2/cm^{-1}$
107	107	107	105	B_2	104,[25] 106[24]
127	128	126	123	A_1	122,[24] 125[25]
169	–	–	–	E and/or B_2	169,[24] 170[25]
175	–	–	–	E and/or B_2	170[25]
299	297	–	–	E and/or B_2	295[26]

3.5. Optical property

The UV-Vis absorption spectra of $CuIn_{1-x}Ce_xTe_2$ powders are shown in Fig. 7. In the inset of Fig. 7, Ce doped into CICT induces an increase of 36.4% in absorption intensity. Therefore, the sample with Ce doping has a larger band gap and absorption efficiency.

As the absorbance A_b is determined by the following equation:

$$A_b = \alpha c l, \tag{3}$$

where α, c, and l are absorption coefficient, concentration of absorption material, and thickness of the liquid layer, respectively. The c and l are determined experimentally, the absorbance A_b is in direct proportion to the absorption coefficient α. Therefore, the value of absorption coefficient α can be determined from the absorption data.

The optical energy band gap E_g is obtained based on the following equation:

$$\alpha h\nu = A(h\nu - E_g)^n, \tag{4}$$

where α and ν are the absorption coefficient and photon frequency respectively; A and n are constants. A depends on temperature and photon energy,[29] and the values of the exponent n, in this case, should be 1/2 due to the direct transition of CICS compounds. Combined with Eq. (3), the equation to determine the optical energy band gap E_g can be written as

$$(A_b h\nu)^2 = A^2 c^2 l^2 (h\nu - E_g). \tag{5}$$

A plot of $(A_b h\nu)^2$ versus $h\nu$ is expected to be a straight line whose intercept on the X axis gives the optical band-gap. That is, the optical band gap E_g value for CICT is determined by extrapolating the linear portion of the curve to the X axis, the cross point in the X axis corresponds to E_g value. The E_g values are 1.28 eV for $CuIn_{0.9}Ce_{0.1}Te_2$ and 1.16 eV for $CuInTe_2$, respectively. It seems that the Ce doped into CICT increases the band gap. This phenomenon might be due to the weak effect of the stretching force in the Te–(In, Ce) bond due to the extension of the Te–(In, Ce) bond length induced by the substitution of Ce for In.

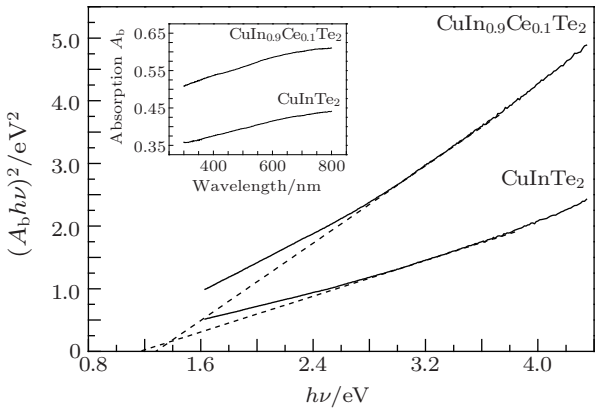


Fig. 7. UV-Vis absorption spectra of $CuInTe_2$ and $CuIn_{0.9}Ce_{0.1}Te_2$ powders.

3.6. Electric property

The temperature dependences of the resistivity of $CuInTe_2$ and $CuIn_{0.9}Ce_{0.1}Te_2$ in a temperature range from 5 K to room temperature are shown in Fig. 8. The resistivities decrease with an increase in temperature, indicating that two of them are typical semiconductors and Ce doping does not change the electric property of $CuInTe_2$.

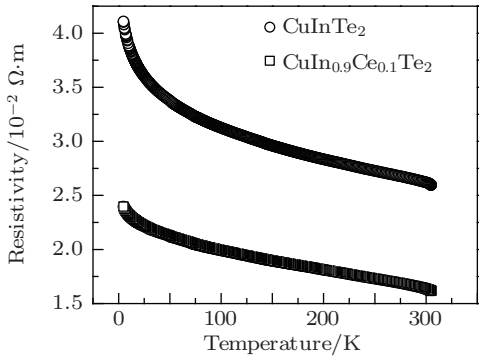


Fig. 8. The temperature dependences of resistivity for $CuInTe_2$ and $CuIn_{0.9}Ce_{0.1}Te_2$ compounds.

4. Conclusions

Ce-doped $CuInTe_2$ powders for thin film solar cells are successfully synthesized by arc-melting. FESEM studies show that the particles of CICT tend to be agglomerated from small to large sizes ranging from 200 nanometers to 5 micrometers. The grain sizes of CICT decrease with an increase of Ce content, implying that cerium doped into CICT is helpful for re-

fining the grains. $CuIn_{1-x}Ce_xTe_2$ crystallizes into a tetragonal chalcopyrite structure (space group I-42d) with a predominant orientation along the [112] direction. The atomic occupations in one unit cell correspond to the 4*a* (0, 0, 0) crystal site for Cu atoms, the 4*b* (0, 0, 0.5) site for In/Ce atoms and the 8*d* (x, 0.25, 0.125) site for Te. Ce partly substitutes for In. The lattice parameters are $a = 6.190(6)$ Å–6.193(0) Å and $c = 12.406(5)$ Å–12.409(5) Å. XPS analysis shows that the valence of Ce can be described as a mixture of valence 4+ and 3+, and the main state might be valence 4+.

Raman spectra shows that the strongest lines appear at 127 cm^{-1}, 128 cm^{-1}, 126 cm^{-1}, 123 cm^{-1} for CICT with $x = 0$, 0.1, 0.2, 0.3, respectively. This is evidently due to the totally symmetric A_1 mode which is the strongest line generally observed in the Raman spectra of the chalcopyrites. The lines at 169 cm^{-1}, 175 cm^{-1}, and 299 cm^{-1} observed only in $CuInTe_2$ without Ce doping are all assigned to E and/or B_2 modes. UV-Vis spectra reveal that E_g values are 1.28 eV for $CuIn_{0.9}Ce_{0.1}Te_2$ and 1.16 eV for $CuInTe_2$, respectively. Ce doping does not change the electric property of $CuInTe_2$. The effects on Raman spectra, E_g and electric properties of Ce doped into CICT could be understood by the weak effect of stretching forces on the Te–(In, Ce) bond due to the extension of Te–(In, Ce) bond length induced by the substitution of Ce for In.

References

[1] Yassitepe E, Shafarman W N and Shah S I 2014 *J. Solid State Chem.* **213** 198

[2] Wu S M, Xue Y Z, Zhou L M, Liu X and Xu D Y 2014 *J. Alloys Compd.* **600** 96

[3] Hsu H R, Hsu S C and Liu Y S 2012 *Solar Energy* **86** 48

[4] Park S W, Kim D I, Lee T S, Lee K U, Yoon Y, Cho Y H, Kim J H, Ahn K M, Lee K J and Jeon CW 2014 *Solar Energy Materials and Solar Cells* **125** 66

[5] Lakhe M and Chaure N B 2014 *Solar Energy Materials and Solar Cells* **123** 122

[6] Chen D S, Yang J, Xu F, Zhou P H, Du H W, Shi J W, Yu Z S and Zhang Y H 2013 *Chin. Phys. B* **22** 018801

[7] Li W, Zhao Y M, Liu X J, Ao J P and Sun Y 2011 *Chin. Phys. B* **20** 068102

[8] Jackson P, Hariskos D, Lotter E, Paetel S, Wuerz R, Menner R, Wischmann W and Powalla M 2011 *Progress in Photovoltaics: Research and Applications* **19** 894

[9] Bodnar' I V, Gurin V S, Solove I N P and Molochko A P 2007 *Semiconductors* **41** 939

[10] Kim S, Kang M, Kim S, Heo J H, Noh J H, Im S H, Seok S I and Kim S W 2013 *ACS Nano* **7** 4756

[11] Orts J L, Díaz R, Herrasti P, Rueda F and Fatás E 2007 *Solar Energy Materials and Solar Cells* **91** 621

[12] Roy S, Bhattacharjee B, Kundu S N, Chaudhuri S and Pal A K 2002 *Mater. Chem. Phys.* **77** 365

[13] Kawano K, Hong B C, Sakamoto K, Tsuboi T and Seo H J 2009 *Opt. Mater.* **31** 1353

[14] Lian H Z, Hou Z Y, Shang M M, Geng D L, Zhang Y and Lin J 2013 *Energy* **57** 270

[15] Atyaoui M, Dimassi W, Atyaoui A, Elyagoubi J, Ouertani R and Ezzaouia H 2013 *J. Lumin.* **141** 1

[16] Li Q B, Lin J M, Wu J H, Lan Z, Wang Y, Peng F G and Huang M L 2013 *J. Lumin.* **134** 59

[17] Lei H W, Zhang H, Gong M and Wu W D 2012 *Chin. Phys. Lett.* **29** 126801

[18] Yakushev M V, Mudryi A V, Martin R W and Feofanov Y 2003 *Mater. Sci. Eng. B* **105** 175

[19] Fu L, Guo Y Q and Zheng S 2014 *J. Alloys Compd.* **591** 304

[20] Hill R J and Howard C J 1987 *J. Appl. Crystallography* **20** 467

[21] Ananthan M R and Kasiviswanathan S 2009 *Solar Energy Materials and Solar Cells* **93** 188

[22] Takahiro M and Tokio N 2010 *Thin Solid Films* **518** 5604

[23] Holah G D, Webb J S and Montgomery H 1974 *J. Physics C: Solid State Phys.* **7** 3875

[24] Rincon C, Wasim S M, Marn G, Huntzinger J R, Zwick A and Galibert J 1999 *J. Appl. Phys.* **85** 3925

[25] Rincon C, Wasim S M, Marn G, Hernandez E, Delgado J M and Galibert J 2000 *J. Appl. Phys.* **88** 3439

[26] Neumann H, Kissinger W, Tomlinson R D and Avgerinos N 1982 *Phys. Status Solidi* **112** K19

[27] Miller A, MacKinnon A and Weaire D 1981 *Solid State Phys.* **36** 119

[28] Neumann H 1985 *Helvetica Physica Acta* **58** 337

[29] Hankare P P, Rathod K C, Chate P A, Jadhav A V and Mulla I S 2010 *J. Alloys Compd.* **500** 78